INTERNATIONAL JOURNAL OF AUTOMOTIVE AND MECHANICAL ENGINEERING
ISSN: 2229-8649 e-ISSN: 2180-1606
VOLUME 23, ISSUE 1, 2026, 13146 - 13160
DOI: https://doi.org/10.15282/ijame.23.1.2026.1.0999

RESEARCH ARTICLE

# Transient thermohydrodynamic of turbocharger thrust bearings with circumferential V-grooves

**Puttha Jeenkour***

Department of Mechanical Engineering, Faculty of Engineering, Burapha University, Chonburi, Thailand

**Abstract** – The primary objective of this paper is to numerically analyze the effect of circumferential V-grooves on the thermohydrodynamic performance of turbocharger thrust bearings, with a focus on lubricant temperature distribution and variation. To investigate the relationship between shaft speed and lubricant temperature, a thermohydrodynamic lubrication model was employed to obtain numerical results. The numerical methodology utilizes the finite difference method coupled with the Newton-Raphson scheme to solve the nonlinear modified Reynolds and energy equations concurrently. To ensure accuracy, steady-state numerical predictions of pressure and temperature distributions were validated against existing research. Subsequently, the numerical findings, focusing on oil pressure, friction, and oil temperature under varying shaft speeds, are thoroughly discussed. The numerical findings indicate that the implementation of grooved thrust bearings with a 5 μm clearance reduces the average lubricant temperature in the contact area by 14% at maximum operating speeds, while maintaining friction levels comparable to those of ungrooved counterparts. However, an excessive increase in groove width and depth adversely affects the bearing's load-carrying capacity and results in higher peak temperatures at the bearing plate edge, especially at widths and depths greater than 30 μm.

**Article History**
Received : 21 May 2025
Revised : 16 November 2025
Accepted : 09 December 2025
Published : 02 March 2026

**Keywords**
*Thermo-hydrodynamic*
*Thrust bearing*
*V-groove*
*Turbocharger*
*Speed-up*

## 1. Introduction

Thrust bearings are essential components in machinery designed to handle axial loads and are used in diverse applications, including automobiles, ship propellers, and small-scale manufacturing. In modern automotive engineering, the trend towards engine downsizing for enhanced energy efficiency and reduced emissions has led to the widespread adoption of turbochargers in eco-friendly vehicles. However, the elevated operating temperatures associated with turbochargers pose a significant challenge to lubrication efficiency. Effective oil lubrication beneath the sliding surfaces, typically forming pressure distributions between the runner and pad surfaces, is crucial for preventing material wear. The oil film that separates the runner and pad surfaces supports the axial load, and its load-carrying capacity is directly related to the pressure within the film [1]. Insufficient oil pressure can cause the oil film to break down, leading to boundary lubrication. Under boundary lubrication conditions, friction at the bearing surface increases sharply, accelerating material wear. Notably, in automotive turbochargers, the compressor operates at remarkably high speeds, ranging from 4 to 35 times the engine speed [2]. Consequently, at a typical engine speed of 3,000 rpm, the compressor speed can vary by up to 93,000 rpm. These extreme operating conditions significantly influence the characteristics of fluid film lubrication, including oil temperature, oil pressure, and friction. Therefore, investigating the lubrication characteristics of thrust bearings under speed-up conditions is of paramount importance.

Recent research on thrust bearings has primarily focused on numerical calculation methods for lubrication, which can be broadly categorized into two main approaches. The first approach involves solving the modified Reynolds equation, often employing finite-difference methods coupled with the Newton-Raphson method to approximate derivative terms and address the inherent nonlinearity of the equations [3-6]. The second, increasingly popular approach leverages the Navier-Stokes equations and the finite element method, facilitated by the availability of commercial software for computation and mesh generation [7-10]. However, the fundamental theory of lubrication continues to evolve to elucidate complex phenomena such as cavitation, viscous flow behavior, thermal effects, and turbulent flow regimes [11-14]. In terms of bearing design, much of the prior work has focused on tailoring bearings for specific applications. For instance, studies have focused on designing bearings to mitigate turbocharger shaft vibration, reduce friction, and enhance load-carrying capacity [15-20]. Bearing geometry, including modifications to the bearing surface, plays a critical role in lubrication performance, making the study of grooved bearings particularly relevant. Zhang et al. [21] experimentally investigated the effect of spiral groove thrust bearings in a cryogenic turbo expander using gas lubrication. Their findings indicated a 7.6% increase in load capacity compared to conventional thrust bearings. Lin et al. [22-23] proposed a high-speed water-lubricated spiral-groove thrust bearing and reported that the spiral groove angle significantly affected the bearing stiffness coefficients, whereas cavitation had a less pronounced impact on the damping coefficient. However, those prior studies were limited by their focus on water-based lubricants and by their calculation of stiffness and damping coefficients. Crucially, they neither discussed the resultant thermohydrodynamic performance, particularly the temperature field, nor applied their findings to turbocharger operating conditions. Research efforts focused on improving thrust bearing performance through means other than surface design can be summarized as follows: [24–26] designed the bearing with multi-layered pads, incorporating an elastic intermediate layer. Consequently, the lubrication behavior was predicted using a thermo-elastic-hydrodynamic model. However, this analysis was limited to steady-state conditions and

*CORRESPONDING AUTHOR | P. Jeenkour | ✉ puttha@eng.buu.ac.th

utilized air as the lubricant. Subsequently, Chong et al. [27] investigated turbocharger lubrication using a thermohydrodynamic (THD) model. Following this, Dong et al. [28] analyzed the effect of a three-lobe semi-floating ring bearing on the THD performance of a turbocharger journal bearing. Crucially, both studies primarily focused on analyzing the temperature distribution in the journal bearing under steady-state operation. Furthermore, Bhat et al. [29] proposed a thrust bearing design incorporating an embedded cooling pipe to reduce surface temperature. However, all the studies focused solely on steady-state analysis. Elevated operating temperatures in the turbocharger significantly limit lubricant efficiency and lifespan. This is evidenced by maintenance guidelines for small-displacement (e.g., 1,000 cc) turbocharged engines, which commonly recommend shorter oil change intervals (e.g., from 10,000 km to 7,000 km) than their naturally aspirated counterparts. Consequently, investigating the thermal behavior of the thrust bearing and developing novel temperature mitigation techniques represent key challenges addressed by the present study.

Drawing upon the limitations of prior research, this study addresses two critical gaps: the analysis of thrust bearing performance under unsteady (transient) conditions and the investigation of the circumferential V-groove design. This work particularly focuses on the circumferential V-groove, which differs from the spiral groove in that the latter partially impedes the lubricant flow in the circumferential direction. The V-groove geometry is known to promote pressure relief along the groove [30]; hence, it is hypothesized that this feature will also lead to a consequential reduction in lubricant temperature. Based on these premises, the current article specifically focuses on studying the thermohydrodynamic characteristics of the circumferential V-groove under transient operation. Therefore, this study investigates the influence of circumferential V-grooves on oil pressure, oil temperature, friction, and load capacity under speed-up conditions. The lubricant is treated as a compressible, viscous fluid, and a transient thermohydrodynamic lubrication model is employed to analyze bearing characteristics. The effects of fixed and free bearing clearances, as well as groove dimensions, are also considered.

## 2. Materials and Methods

### 2.1 Themohydrodynamic Lubrication Model with V-Grooves

#### *2.1.1 Operation of turbocharger and thrust bearing geometry*

Figure 1 illustrates the operation of a turbocharger. Exhaust gas from the engine cylinders flows into a turbine, causing the shaft connected to a compressor to rotate. Simultaneously, ambient air is drawn in and compressed by the compressor. Subsequently, this compressed air is directed into the engine cylinders. The rotating shaft relies on thrust bearings for axial force support, and these bearings are typically mounted on the compressor side of the shaft.

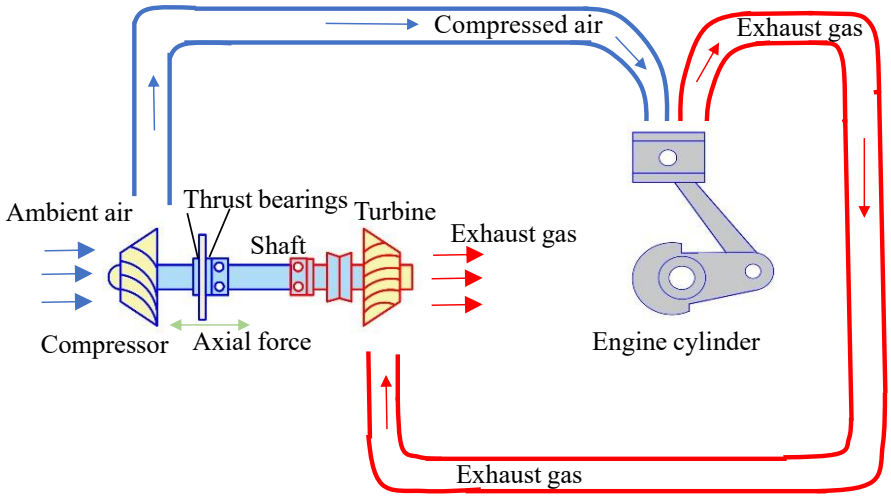


Figure 1. Schematic representation of the turbocharger operation

The pad shape significantly influences the bearing's axial load-carrying capacity. Figure 2 illustrates the bearing geometry, presenting the top view, section view A-A, and section view B-B. As depicted in Figure 2(a), the pad is modified with V-grooves. The notations $S_n, \theta_0, r_{g1}$ and $r_{g2}$ represent the taper height, the pad angle, the first groove radius, and the second groove radius, respectively. The pad width is determined by the difference between the outer pad radius ($r_{out}$) and the inner pad radius ($r_{in}$). The pad area is divided into two regions: region I, an inclined pad, and region II, a flat pad. The length of the inclined region (Region-I) is defined by a circumferential angle of $0.7\theta_0$, while the pad pitch angle in Figure 2(b) is defined as $\alpha$. The high speed of the runner surface ensures that the runner and pad surfaces are separated by a hydrodynamic film thickness, $h(\theta_i,r_i)$, at any given position on the pad. This film thickness can be analytically expressed as Eq. (10.

$$h(\theta_i, r_i) = \begin{cases} h_0 + r_i(0.7\theta_0 - \theta_i)tan\alpha + |\delta(\theta_i, r_i)| & ; 0 \le \theta_i \le 0.7\theta_0 \\ h_0 & ; \theta_i > 0.7\theta_0 \end{cases} \quad (1)$$

where $h_0$ represents the minimum oil film thickness, which is also known as the bearing clearance. The pad pitch angle, $\alpha$, is given by $\alpha = \tan^{-1}(S_n/0.7r_i\theta_0)$, where $S_n$ and $\theta_0$ are previously defined parameters. The groove shape, denoted by $\delta$,

is determined by the groove width ($w_g$), the groove depth ($d_g$), and the groove radius ($r_g$). The calculation of the groove shape on the pad surface, as illustrated in Figure 2(c), is as Eq. (2).

$$\delta(\theta_i, r_i) = \begin{cases} -\left(\dfrac{d_g}{0.5w_g}\right)\left(0.5w_g - |r_i - r_{gk}|\right) \\ \text{for} \quad (r_{gk} - 0.5w_g) \le r_i \le r_{gk}; \;\; k = 1,2 \\ -d_g + \left(\dfrac{d_g}{0.5w_g}\right)(r_i - r_{gk}) \\ \text{for} \quad r_{gk} \le r_i \le (r_{gk} + 0.5w_g); k = 1,2 \end{cases} \tag{2}$$

where $i$ indicates the position considered within the contact interface, and $k$ = 1, 2 refers to the 1st and 2nd grooves, respectively.

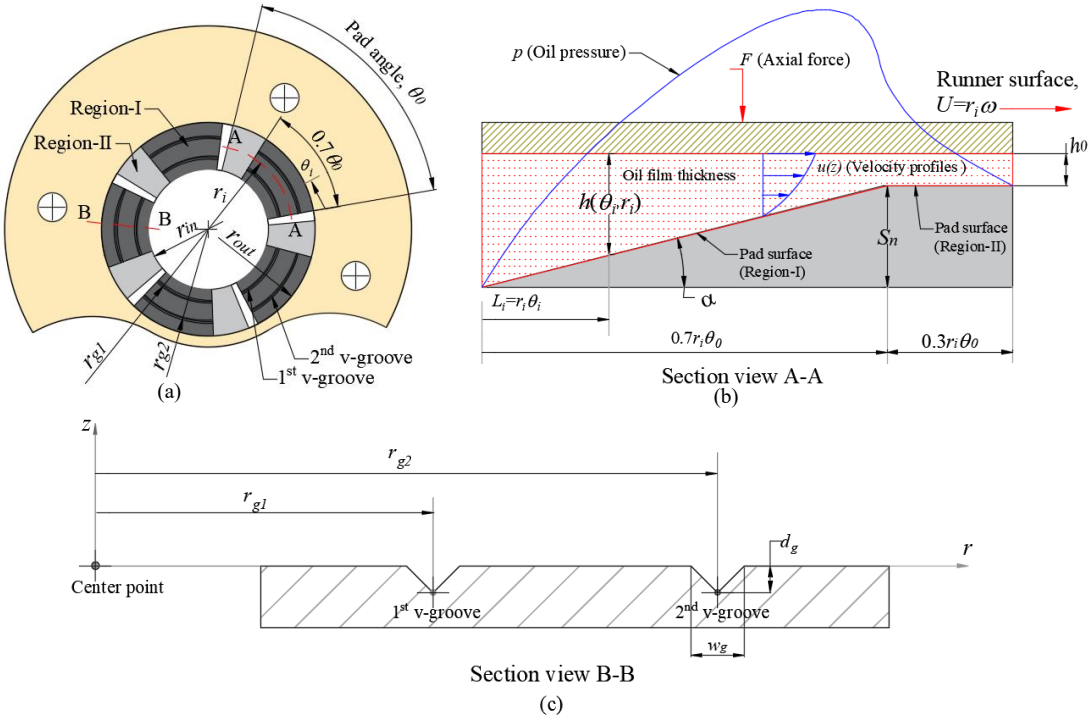


Figure 2. Thrust bearing geometry: (a) top view, (b) section view A-A, and (c) section view B-B

### *2.1.2 Oil pressure distribution*

As shown in Figure 2(b), a sliding surface with velocity $U$ generates an oil pressure distribution, $p$, within the contact interface. The oil pressure values are determined using the modified time-dependent Reynolds equation in the $\theta$-$r$ coordinate system, as presented in Eq. (3).

$$\frac{1}{r}\frac{d}{d\theta}\left(\frac{\rho h^3}{12\eta\, r}\frac{dp}{d\theta}\right) + \frac{d}{dr}\left(\frac{\rho h^3}{12\eta\, r}\frac{d(p.r)}{dr}\right) - \left(\frac{U}{2r}\right)\frac{d(\rho h)}{d\theta} - \frac{d(\rho h)}{dt} = 0 \tag{2}$$

where $\eta$ represents the oil viscosity and $\rho$ represents the oil density. Since the oil properties are temperature- and pressure-dependent, the oil viscosity and density are calculated using Eq. (4) and Eq. (5), respectively.

$$\eta = \eta_0 exp\{(ln\eta_0 + 9.67)(-1 + [1 + 5.1 \times 10^{-9} p]^z) - \gamma(T - T_0)\} \tag{4}$$

$$\rho = \rho_0\left(1 + \frac{0.6 \times 10^{-9}.p}{1 + 1.7 \times 10^{-9}.p}\right)(1 - \beta\{T - T_0\}) \tag{5}$$

The constant values $\eta_0$, $z$, $\rho_0$, $\gamma$, and $\beta$ are obtained from oil testing [1, 31]. Here, $T$ represents the oil temperature, and $T_0$ is the ambient temperature. The runner speed also influences the oil pressure. During vehicle acceleration, the engine demands greater power to increase its velocity, consequently raising the rotational speed ($\omega$) of the turbocharger rotor. This rapid increase in speed is commonly referred to as the speed-up condition. Under this speed-up condition, the rotational speed is assumed to be a linear function of the initial speed ($\omega_i$) and time ($t$). Consequently, the surface velocity at a specific point within the contact interface is determined as:

$$U(t) = r_i\left(\omega_i + \left[\frac{\Delta\omega}{\Delta t}\right]t\right) \tag{6}$$

The axial force is determined by integrating the oil pressure distribution over the contact area, based on the equilibrium of forces in the axial direction. Therefore, the total axial force ($F$) acting on $N$ pads is given by the following integration:

$$F = N \int_0^{\theta_0} \int_{r_{in}}^{r_{out}} p(r,\theta) r dr d\theta \tag{7}$$

***2.1.3 Oil temperature distribution***

Due to the fluid's viscosity and shear strain rate, the temperature rise significantly affects lubrication efficiency. In the circumferential ($\theta$) and radial ($r$) directions, the high rotational speeds of the turbocharger lead to high lubricant velocities within the bearing clearance. Consequently, the primary mechanism of heat transfer in these directions is convection, which significantly outweighs conduction. For thin-film fluid dynamic systems operating at high flow rates, neglecting longitudinal (or radial) conduction simplifies the model while maintaining reasonable accuracy by focusing on the dominant convective transport. While heat conduction across the film thickness (the $z$-direction) is typically essential for accurately modeling heat transfer to the bearing surfaces, it is neglected here based on the specific focus of this study: rapid speed-up conditions over an extremely short duration (i.e., less than 10 seconds). During this short transient phase, viscous dissipation (shear heating) is the dominant thermal driving force, leading to a rapid, localized increase in lubricant temperature. The limited time frame is insufficient for significant heat transfer by conduction between the lubricant bulk and the solid surfaces, especially given the high rate of heat generation from shearing. Therefore, within this short transient window, the lubricant's thermal behavior is assumed to be primarily dictated by convection (in $\theta$and $r$) and viscous dissipation, thus justifying the simplification for computational tractability and effective analysis of the transient response. Furthermore, Chatzisavvas [31] compared the predicted bearing temperature for both the conduction-neglected and conduction-included cases for a thrust bearing. The findings indicated that while a slight quantitative difference existed, the overall trends and qualitative characteristics of the temperature distribution remained consistent between the two modeling approaches. Therefore, neglecting heat conduction is considered a reasonable simplification for the purpose of identifying key performance trends and the comparative analysis of V-groove geometry in this study. To predict the temperature profile ($T$) within the contact interface, the energy equation is employed under the following assumptions: neglecting heat conduction, entropy effects, and heat sources. Consequently, the two-dimensional form of the energy equation can be expressed as:

$$\rho c_p \left( \frac{dT}{dt} + \bar{u}_r \frac{dT}{dr} + \frac{\bar{u}_\theta}{r} \frac{dT}{d\theta} \right) = \eta \left\{ \left( \frac{du_r}{dz} \right)^2 + \left( \frac{du_\theta}{dz} \right)^2 \right\} \tag{8}$$

where $c_p$ represents the specific heat capacity of the lubricant being tested. The oil velocity profiles in the radial ($u_r$) and angular ($u_\theta$) directions are given by:

$$u_r = \frac{1}{2\eta} \frac{dp}{dr} (z^2 - zh) \tag{9}$$

$$u_\theta = \frac{1}{2\eta\, r} \frac{dp}{d\theta} (z^2 - zh) + \left( \frac{z}{h} \right) U \tag{10}$$

Therefore, the average oil velocity across the oil film thickness in the radial direction ($\bar{u}_r$) and the average oil velocity in the angular direction ($\bar{u}_\theta$) are calculated as follows:

$$\bar{u}_r = \frac{1}{h} \int_{z=0}^{z=h} u_r \, dz \tag{11}$$

$$\bar{u}_\theta = \frac{1}{h} \int_{z=0}^{z=h} u_\theta \, dz \tag{12}$$

The shear strain rates within the fluid film in the radial and angular directions can be approximated by the ratio of the difference in surface velocities to the oil film thickness. By substituting $z$=$h$ and $z$=0 into Eq. (9) and Eq. (10), the runner surface velocity and the bearing surface velocity can be determined. Consequently, the shear strain rates are expressed as:

$$\frac{du_r}{dz} = \frac{u_r(h) - u_r(0)}{h}; \quad \frac{du_\theta}{dz} = \frac{u_\theta(h) - u_\theta(0)}{h} \tag{13}$$

***2.1.4 Frictional torque***

As is well known, material wear is influenced by friction. Therefore, it is important to determine the friction within the contact interface. Since friction arises from the shear strain rates within the fluid film, the frictional torque acting on the bearing surface is given by:

$$F_b = N \int_{\theta_{in}}^{\theta_{out}} \int_{r_{in}}^{r_{out}} r \times \eta \left( \frac{du_\theta}{dz} \right)_{z=0} r dr d\theta \tag{14}$$

The frictional torque at a runner surface is expressed as Eq. (15).

$$F_r = N \int_{\theta_{in}}^{\theta_{out}} \int_{r_{in}}^{r_{out}} r \times \eta \left(\frac{du_\theta}{dz}\right)_{z=h} r dr d\theta \tag{15}$$

**2.2 Numerical Procedure**

This part describes the steps for numerical calculation to solve the oil pressure and oil temperature distributions. Firstly, the equations mentioned above must be rewritten in dimensionless form. The following dimensionless parameters are adopted to rewrite the above equations into dimensionless form: $P = p/p_0$, $p_0 = \eta_0 r_m \omega_i r_0 \theta_0 / h_0^2$, $H = h/h_0$, $R = r/r_0$, $\Theta = \theta/\theta_0$, $t^* = t/t_0$, $r_0 = r_{out} - r_{in}$, $r_m = r_{in} + 0.5r_0$, $\eta^* = \eta/\eta_0$, $\rho^* = \rho/\rho_0$, and $T^* = T/T_0$. The dimensionless Reynolds equation and the dimensionless energy equation are presented as examples in Eq. (16) and Eq.(17), respectively.

$$f_P = \frac{1}{R}\frac{d}{d\Theta}\left(K\frac{dP}{d\Theta}\right) + \theta_0^2 \frac{d}{dR}\left(K\frac{d(PR)}{dR}\right) - \Lambda_1 \frac{d(\rho^* H)}{d\Theta} - \Lambda_2 \frac{d(\rho^* H)}{dt^*} \tag{16}$$

$$f_T = \left\{\psi_1\left(\frac{H^2}{\eta^* R^2}\right)\frac{dP}{d\Theta} - \psi_2\left(\frac{1}{R}\right)\right\}\frac{dT^*}{d\Theta} + \psi_3\left(\frac{H^2}{\eta^*}\right)\frac{dP}{dR}\frac{dT^*}{dR} + \psi_4\left(\frac{\eta^*}{\rho^* H^2}\right) - \left(\frac{T_0}{t_0}\right)\frac{dT^*}{dt^*} \tag{17}$$

The notations $K$, $\Lambda_1$, $\Lambda_2$, $t_0$, $\psi_1$, $\psi_2$, $\psi_3$ and $\psi_4$ are defined as follows: $K = \frac{\rho^* H^3}{R\eta^*}$, $H = h/h_0$, $\Lambda_1 = 6\eta_0 r_0 \theta_0 U / h_0 p_0$, $\Lambda_2 = 12\eta_0 r_0^2 \theta_0^2 / h_0^2 p_0 t_0$, $t_0 = t_f - t_i$, $\psi_1 = h_0^2 p_0 T_0 / 12\eta_0 r_0^2 \theta_0^2$, $\psi_2 = UT_0/2r_0\theta_0$, $\psi_3 = h_0^2 p_0 T_0 / 12\eta_0 r_0^2$, and $\psi_4 = \eta_0 U^2 / \rho_0 c_p h_0^2$. Here, $t_i$ represents the initial time, and $t_f$ represents the final time for the speed-up condition. Subsequently, the first- and second-order derivative terms are approximated using the finite difference method. The number of nodes along the radial axis is 168 ($m$ = 168) for one pad, and the number of nodes along the angular axis is 300 ($n$ = 300). Moreover, the use of adaptive grids helps control the number of nodes within each groove area. Thus, the number of nodes in one groove is maintained at (10 ×210) for all varying groove sizes. The Newton-Raphson scheme is employed to solve the nonlinear equations. Consequently, the oil pressure and the oil temperature can be updated based on the previous oil pressure, $P_{i,j}^0$, and the previous oil temperature, $T_{i,j}^0$, as follows:

$$P_{i,j} = P_{i,j}^0 + Re\left(\frac{f_{P,i,j}}{df_{P,i,j}/dP_{i,j}}\right) \tag{18}$$

$$T_{i,j}^* = T_{i,j}^0 + Re\left(\frac{f_{T,i,j}}{df_{T,i,j}/dT_{i,j}}\right) \tag{19}$$

where $Re$ is the under-relaxation factor, with a value between 0 and 1.0. Here, $i$ represents the considered node along the angular axis, and $j$ represents the considered node along the radial axis. The convergence criteria for the dimensionless oil pressure and dimensionless oil temperature are as follows:

$$\epsilon_P = \frac{\sum_{j=1}^{j=m}\sum_{i=1}^{i=n}\left|P_{i,j} - P_{i,j}^0\right|}{\sum_{j=1}^{j=m}\sum_{i=1}^{i=n} P_{i,j}} \leq 1 \times 10^{-5};\ \epsilon_T = \frac{\sum_{j=1}^{j=m}\sum_{i=1}^{i=n}\left|T_{i,j}^* - T_{i,j}^0\right|}{\sum_{j=1}^{j=m}\sum_{i=1}^{i=n} T_{i,j}^*} \leq 1 \times 10^{-5} \tag{20}$$

The boundary conditions used to solve for the oil pressure, where the pressures at the edges of the pad are defined as follows:

$$P(i=1,j) = P(i=n,j) = P(i,j=1) = P(i,j=m) = 0 \tag{21}$$

The boundary conditions used to calculate the oil temperature are as follows:

$$T^*(i=1,j) = T^*(i,j=1) = 0;\ \left(\frac{dT^*}{d\Theta}\right)_{i=n} = \left(\frac{dT^*}{dR}\right)_{j=m} = 0 \tag{22}$$

All the equations mentioned above were implemented in the code programming based on the flowchart shown in Figure 3. The flowchart illustrates the numerical procedure for solving the oil pressure and oil temperature distributions. The process begins by inputting the oil properties and pad geometry, followed by inputting the operating conditions. Next, the algorithm guesses initial values for the oil pressure ($P_{i,j}$) and oil temperature ($T_{i,j}^*$). Based on these initial values, it proceeds to find the parameters $H_{i,j}$, $K_{i,j}$, $\Lambda_1$, and $\Lambda_2$. Subsequently, the oil pressure is updated using Eq. (16) and Eq. (18). In parallel, the algorithm finds the parameters $\psi_1$, $\psi_2$, $\psi_3$ and $\psi_4$. Then, the oil temperature is updated using Eq. (17) and Eq. (19). After updating both pressure and temperature, a convergence check is performed. If the error criteria $\epsilon_P$ and $\epsilon_T$ are greater than 1x10$^{-5}$, the process loops back to the step of updating $P_{i,j}$ and $T_{i,j}^*$ with the newly calculated values. If the convergence criteria are met, the algorithm checks whether the current time ($t^*$) has reached the final time ($t^*_f$). If not, the time and velocity are updated. The previous pressure and temperature values are then set to the current values ($P_{i,j}^0 = P_{i,j}$, $T_{i,j}^0 = T_{i,j}^*$), $t^{*0} = t^*$), and the process loops back to finding $H_{i,j}$, $K_{i,j}$, $\Lambda_1$, and $\Lambda_2$ with the updated conditions. Once the final time ($t^* = t^*_f$) is reached, the algorithm proceeds to output the results and stop.

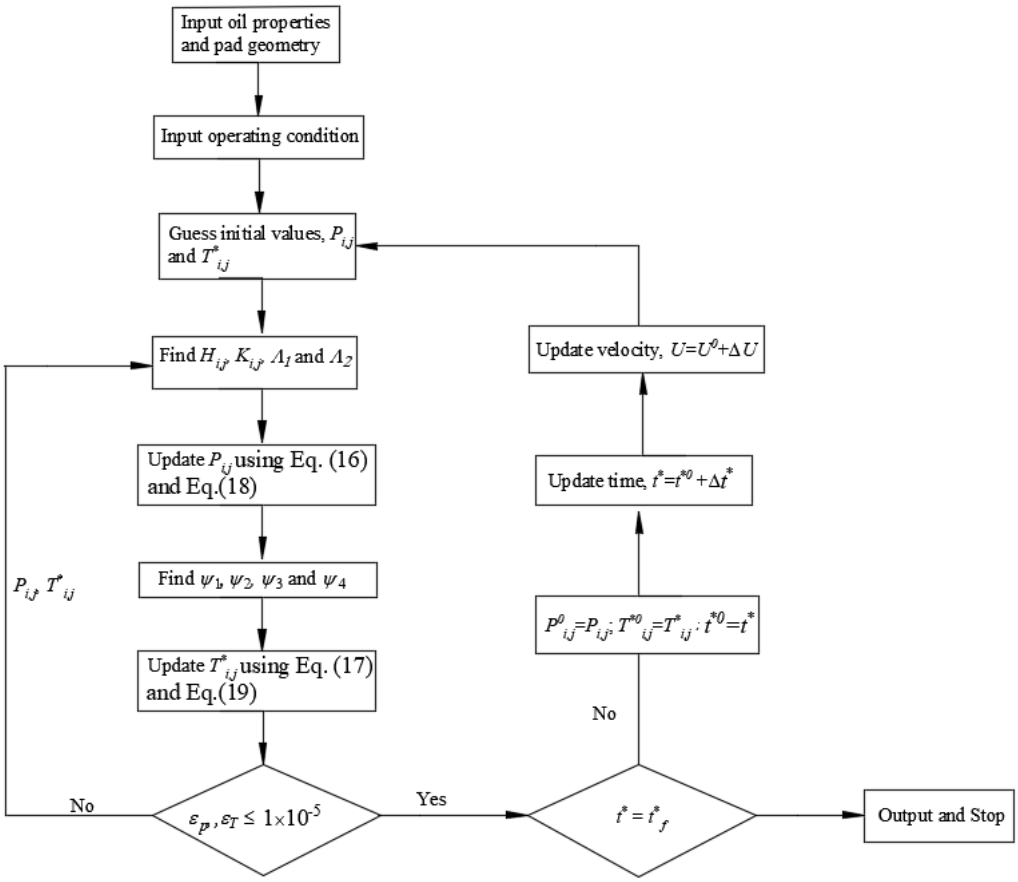


Figure 3. Flowchart of a computation

## 3. Results and Discussion

This section presents the numerical results, considering the effect of V-grooves on the oil pressure distributions, fluid film temperature, axial force, and frictional torque. The results presented in this section were obtained based on the thrust bearing dimensions and the operating conditions, along with the oil properties listed in Tables 1 and 2, respectively. Firstly, the numerical procedure was verified against previous results reported in [31] under steady-state conditions. The specific condition chosen for comparison involved a rotational velocity of 20,000 rad/s (equivalent to 190,986 rpm) and a minimum oil film thickness (bearing clearance, $h_0$) of 5.0 μm. Figure 4 presents example results from this study in 3-dimensional plots. The pressure and temperature profiles for the pads without a groove, shown in Figure 4(a) and Figure 4(c), exhibit similar shapes to those reported in previous works. The maximum temperature is observed at the pad exit, where the oil film thickness is at its minimum. For V-grooves, illustrated in Figure 4(b) and Figure 4(d), both pressure and temperature decrease within the groove regions. When the pad surface incorporates grooves, the oil film thickness in these regions becomes greater than that of a flat pad. Consequently, both pressure and temperature drop at these locations.

Table 1. Thrust bearing dimensions

| Parameters | Values |
|---|---|
| Inner radius of pad, $r_{in}$, (m) | $3.55\times10^{-3}$ |
| Outer radius of pad, $r_{out}$, (m) | $6.30\times10^{-3}$ |
| Pad angle, $\theta_0$, (rad) | $\pi/4$ |
| Number of pads, $N$ | 5 |
| Taper height, $S_n$, (m) | $1.00\times10^{-5}$ |
| Grooved width, $w_g$, (m) | $4.00\times10^{-5}$ |
| Grooved depth, $d_g$, (m) | $4.00\times10^{-5}$ |
| 1st groove position, $r_{g1}$, (m) | $4.25\times10^{-3}$ |
| 2nd groove position, $r_{g2}$, (m) | $5.25\times10^{-3}$ |
| Radius of a central pad, $r_m$, (m) | $4.925\times10^{-3}$ |

Table 2. Oil properties and operating conditions

| Parameters | Values |
|---|---|
| Dynamic oil viscosity, $\eta_0$, (Pa.s) | $7.68\times10^{-3}$ |
| Oil density, $\rho_0$, (kg/m$^3$) | 874.5 |
| Viscosity-pressure index, $z$ | 0.54 |
| Specific heat capacity of oil, $c_p$, (J/kg.ºC) | 2010 |
| Density-temperature coefficient, $\beta$, (1/ ºC) | $7.40\times10^{-4}$ |
| Viscosity-temperature coefficient, $\gamma$, (1/ ºC) | $2.25\times10^{-2}$ |
| Initial rotational velocity, $\omega_i$, (rad/s) | $5.00\times10^{3}$ |
| Final rotational velocity, $\omega_f$, (rad/s) | $30.0\times10^{3}$ |
| Ambient temperature, $T_0$, (ºC) | 30 |
| Final time for speed-up, $t_f$, (s) | 10 |

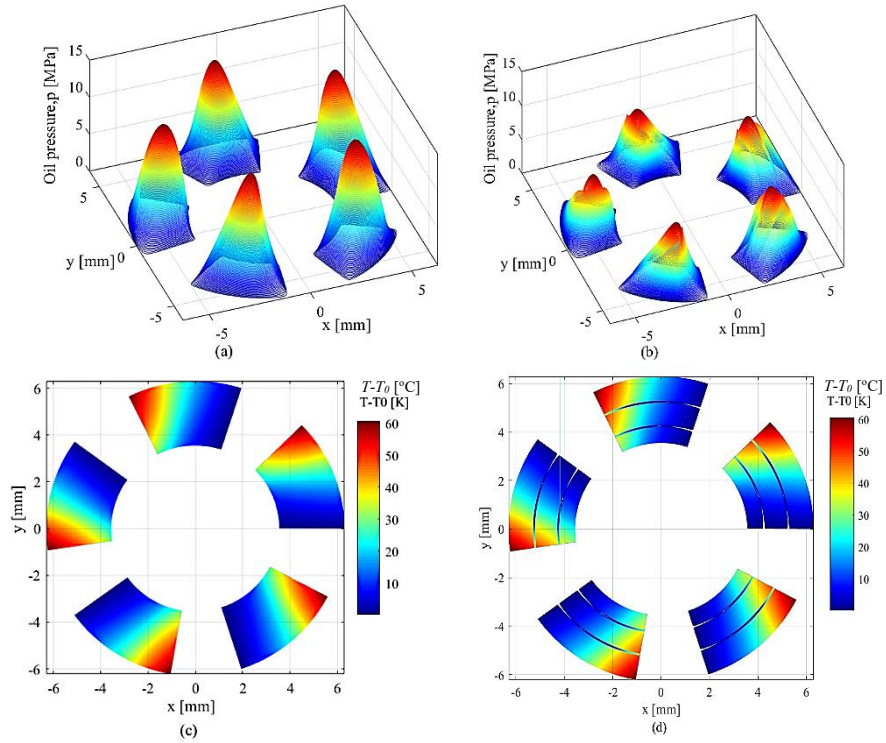


Figure 4. Present calculations for the 3-dimensional graph ($h_0$=5.0 µm, $w_g$=$d_g$=40µm): (a) oil pressure for the normal pads, (b) oil pressure for the v-groove pads, (c) oil temperature for the normal pads, (d) oil temperature for the v-groove pads

The overall pressure is lower compared to that of a grooveless pad. To compare the pressure and temperature values with previous work, these values at the pad center and the pad edge are presented in Figure 5(a) and Figure 5(b), respectively. Considering the pad without a groove, the pressure distributions at $r = r_m$ (pad center) for both the isothermal and thermal models are compared with the 2D full model (previous work). Similarly, the temperature distributions at $r = r_{in}$ and $r = r_{out}$ (pad edge) are compared with the 2D full model. The square and circle markers in Figure 5 were obtained by interpreting the graphs presented by Chatzisavvas [31]. The continuous and dashed lines represent the results from the present study. The current results demonstrate that the pressure and temperature distributions are in good agreement with those reported in previous work. Therefore, this confirms that the numerical procedure described above is efficient and accurate for investigating the effect of V-grooves and the speed-up condition in subsequent calculations. The temperature effect acts as a parameter that reduces pressure buildup within the oil film for a fixed bearing clearance. Thus, the thermal model is appropriate for this study. Secondly, the bearing characteristics under transient conditions are analyzed and presented in this section. According to the study conditions, the compressor's rotational speed increases over 10 seconds. The initial and final rotational velocities are 5,000 rad/s and 30,000 rad/s, respectively. For the bearing without a groove, the pressure and temperature distributions at different time steps are shown in Figures 6 and 7, respectively. The fixed bearing clearance is 5 µm ($h_0$ = 5 µm). The results indicate that the pressure profile is related to the speed-up, with the oil pressure profile forming and increasing gradually as the compressor speed increases. The maximum pressures during the period from 1.0 to 10 seconds range from approximately 5.0 to 20 MPa, representing a four-fold increase from the initial condition.

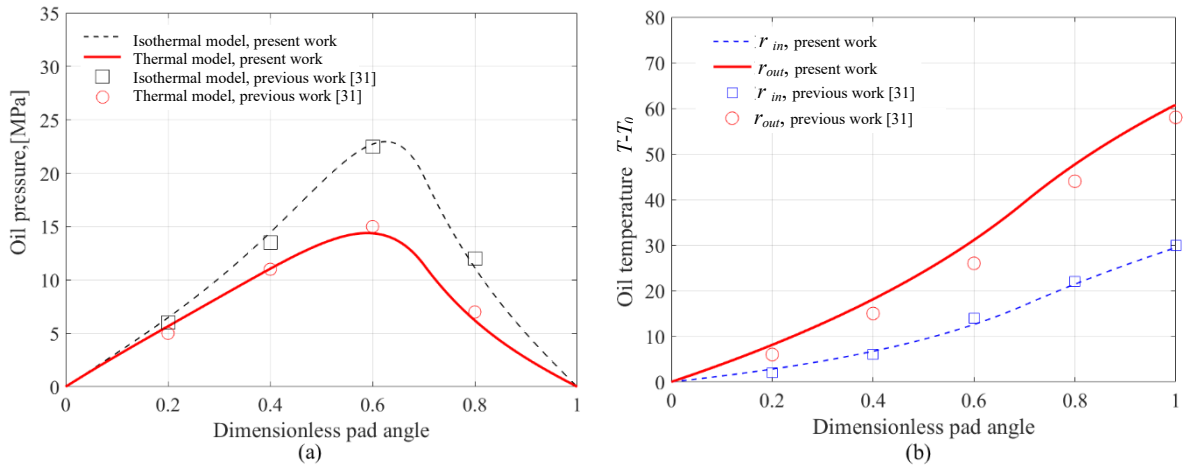


Figure 5. Verification of a numerical computation by the previous work [31] (bearing clearance, $h_0$=5.0 μm) :(a) oil pressure and (b) oil temperature

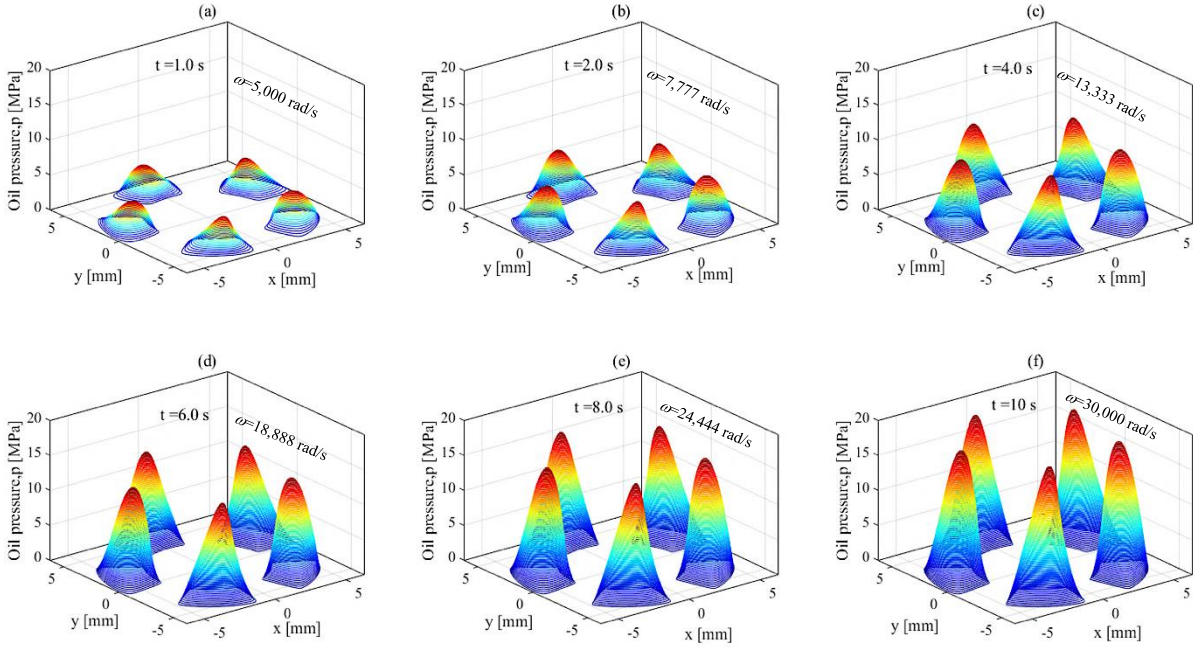


Figure 6. Pressure distributions for a bearing with no groove ($h_0$=5 μm): (a) $t$=1.0 s, (b) $t$=2.0 s, (c) $t$=4.0 s, (d) $t$=6.0 s, (e) $t$=8.0 s, and (f) $t$=10 s

The principles of viscous fluid flow explain this phenomenon. As the compressor speed increases, the velocity of the runner surface also increases, leading to increased oil flow velocity, momentum, and consequently, pressure. Similarly, the temperature increases with the compressor's rotational velocity, as illustrated in Figure 7. The fluid film temperature is related to the fluid's shear rate. Consequently, the increased oil flow velocity resulting from the compressor speed leads to higher shear rates and oil temperatures. The results indicate that the maximum temperatures during the period from 1.0 to 10 seconds are above the ambient temperature, ranging from approximately 23 to 75 ºC. The maximum temperature occurs in the flat pad area at the outer radial location, corresponding to region II as depicted in Figure 1. In this region, the fluid film thickness is at its minimum, which, in turn, affects the variation in the shear rate. Consequently, the maximum temperature is observed in region II. A critical point to consider is the increase in oil temperature during the compressor's speed-up phase. As previously mentioned, this phenomenon directly influences lubrication efficiency. Therefore, the development of lubricants and bearings designed to mitigate this temperature rise is significant.

The pad surface in region I, as depicted in Figure 1, is modified by the addition of two circumferential grooves. Figures 8 and 9 illustrate the distributions of oil pressure and temperature at different time steps during the speed-up process. The groove width is 40 μm, the groove depth is 40 μm, and the fixed bearing clearance is 5 μm (($h_0$ = 5 μm). For the V-grooved pad, the results exhibit the same general trend as for the pad with a normal surface. Furthermore, as the compressor speed increases from 5,000 rad/s to 30,000 rad/s, the pressure and temperature profiles also increase due to the rise in momentum and shear rate, as previously mentioned. The maximum pressure ranges from 3.0 MPa to 14 MPa. Compared to the case without grooves, v-grooves significantly reduce oil pressure across all speeds. Based on the principle of mass conservation, when a pad incorporates v-grooves, the fluid film can flow through them, increasing the cross-sectional area available for fluid flow. Consequently, the overall velocity profile of the oil film decreases, leading

to a drop in lubricant pressure. Regarding the oil temperature, as illustrated in Figure 9, when the bearing clearance is fixed, the maximum temperature and its location remain unchanged compared to the pad without grooves. However, the oil temperature decreases in the v-groove regions because the increased oil film thickness there reduces the shear rate. Consequently, the oil temperature also drops. The numerical results suggest that the average temperature for the pad with grooves is noticeably lower.

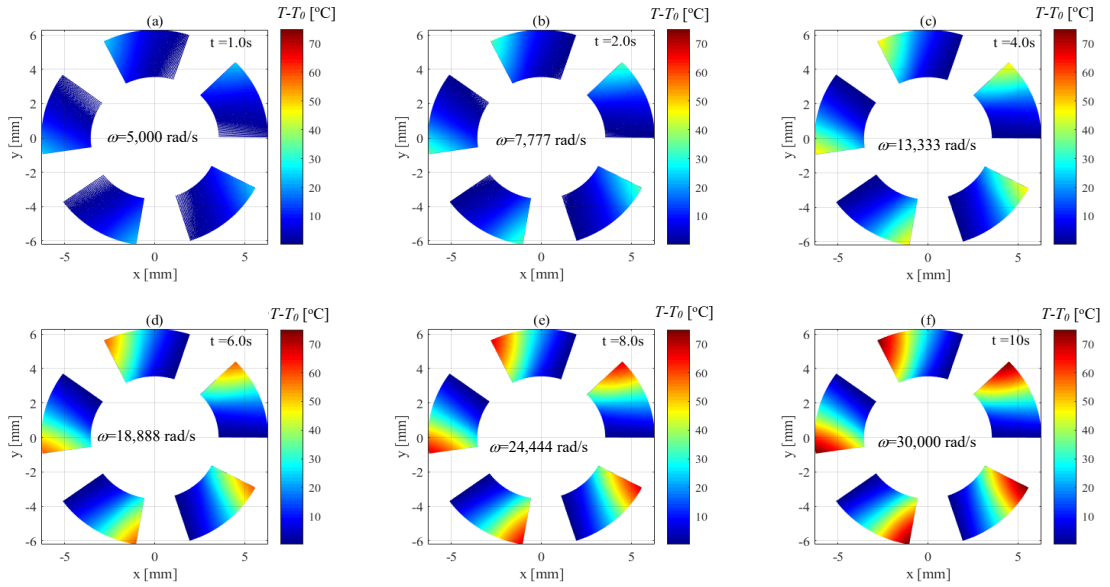


Figure 7. Temperature distributions for a bearing with no groove ($h_0$=5 μm): (a) $t$=1.0 s, (b) $t$=2.0 s, (c) $t$=4.0 s, (d) $t$=6.0 s, (e) $t$=8.0 s, and (f) $t$=10 s

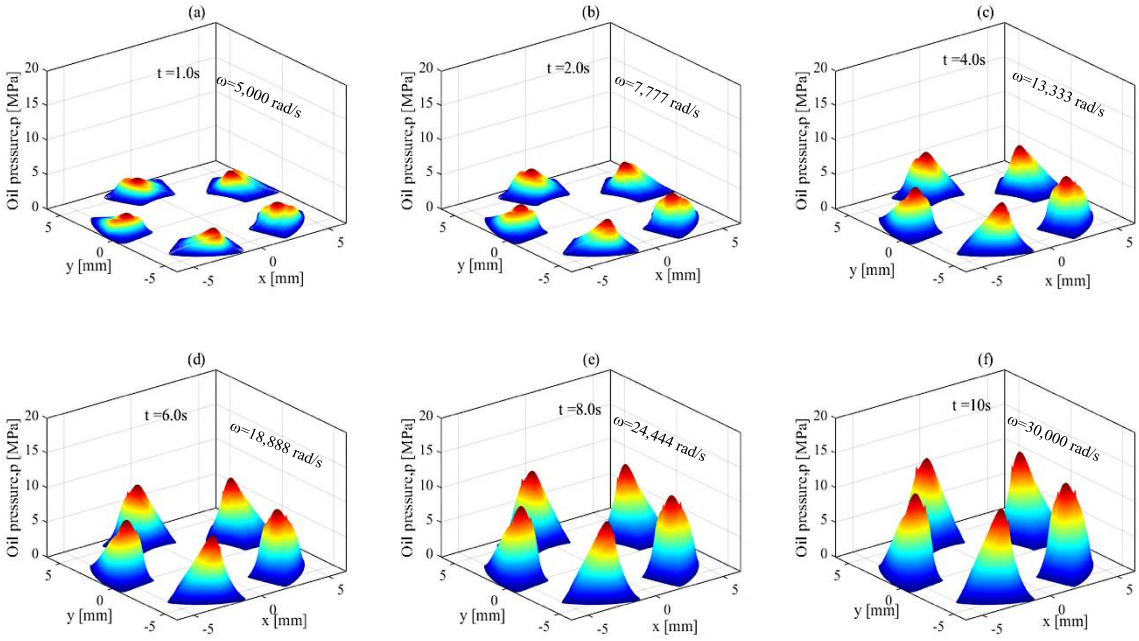


Figure 8. Pressure distributions for a bearing with v-groove ($h_0$=5 μm, $w_g$=40 μm, $d_g$=40 μm): (a) $t$=1.0 s, (b) $t$=2.0 s, (c) $t$=4.0 s, (d) $t$=6.0 s, (e) $t$=8.0 s, and (f) $t$=10 s

To clearly illustrate the comparison and support the aforementioned explanation, the pressure and temperature distributions across the bearing (along cross-section B-B in Figure 2(c)) for both non-grooved and v-grooved bearings are shown in Figure 10. Figure 10(a) illustrates the pressure distribution at a pad angle of $\theta$=π/8 rad and the final time is 10 s. The comparison results further confirm that the bearing with v-grooves experiences lower oil pressure, resulting in lower pressure than the bearing without grooves. Figure 10(b) illustrates the temperature distribution at a pad angle of π/4 rad and the final time is 10 s. The comparison results clearly demonstrate that the bearing with grooves has a lower oil temperature than the one without grooves, particularly in the groove area. In this region, the temperature drops immediately and significantly, distinctly different from the bearing without grooves. Therefore, a thorough investigation

into the effects of groove dimensions, such as depth and width, is significant for determining the advantages and disadvantages of implementing this bearing design in turbochargers.

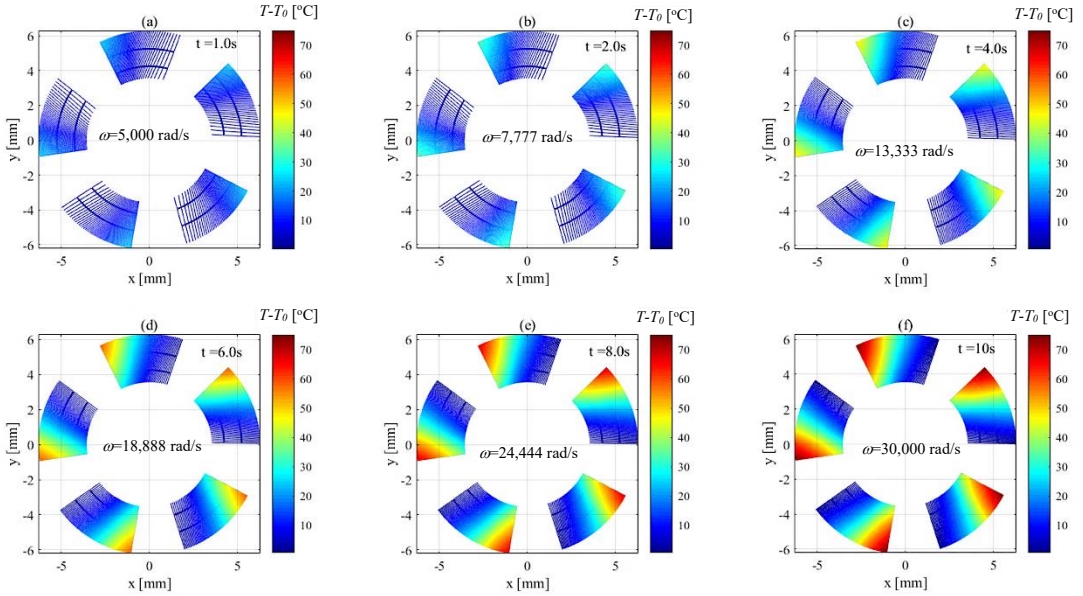


Figure 9. Temperature distributions for a bearing with v-groove ($h_0$=5 µm, $w_g$=40 µm, $d_g$=40 µm): (a) $t$=1.0 s, (b) $t$=2.0 s, (c) $t$=4.0 s, (d) $t$=6.0 s, (e) $t$=8.0 s, and (f) $t$=10 s

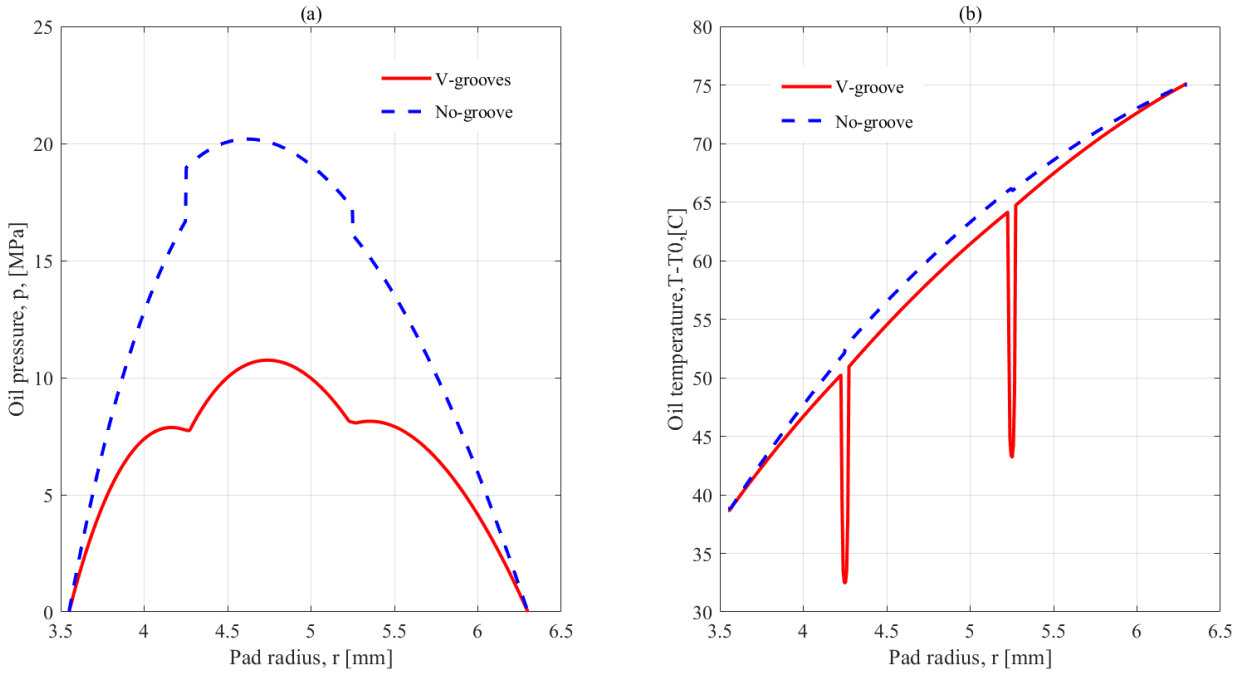


Figure 10. Comparision of thrust bearing behaviours under fixed bearing clearance ($h_0$=5 µm, $t$=10 s, $w_g$=40 µm, $d_g$=40µm): (a) oil pressure at $\theta$=π/8 rad, (b) oil temperature at $\theta$=π/4 rad

Finally, this section discusses bearing characteristics for both fixed and free bearing clearances. Figure 11 illustrates the maximum pressure ($P_{max}$), the average temperature ($T_{avg}$-$T_0$), the load capacity ($F$), the frictional torque at the bearing surface ($F_b$), and the frictional torque at the runner surface ($F_r$). The results shown in Figure 11(b)-11(f) consider the variation in groove sizes under speed-up conditions and a fixed bearing clearance, with the speed-up condition depicted in Figure 11(a). The results indicate that as the compressor speed increases, the values of $P_{max}$, $T_{avg}$ - $T_0$, $F$, $F_b$, and $F_r$ also increase across all the case studies. Regarding the effect of groove size, an increase in groove size leads to a drop in oil pressure within the groove areas due to greater oil entrainment through the grooves. Consequently, the maximum pressure decreases with increasing groove size, as illustrated in Figure 11(b). Groove size also influences the average temperature. Consistent with the reasons discussed previously, the temperature in the groove region is lower because the oil's shear strain rate is reduced. Therefore, for larger groove sizes, the average temperature decreases, as illustrated in Figure 11 (c). Regarding the load capacity shown in Figure 11(d), bearings with larger groove sizes exhibit a lower load capacity compared to those with smaller groove sizes. Consequently, bearings with grooves take longer to reach equilibrium or to

overcome the external load and require higher speeds to generate sufficient oil pressure to resist the axial load. Figure 11(e) and Figure 11(f) illustrate the frictional torque at the bearing surface and the runner surface, respectively. The results indicate that groove size has a minimal effect on frictional torque at the bearing surface, as Fb values remain relatively consistent across all studied groove sizes. Conversely, as the groove size increases, the frictional torque at the runner surface decreases. The differential friction behavior can be explained by examining the shear rate components at each surface. At the groove locations, the local film thickness ($h$) increases, decreasing the Couette flow term ($U/h$) and thereby reducing the shear stress on both surfaces. However, at the stationary bearing surface ($z$=0), the pressure-driven flow (Poiseuille term) ($\frac{1}{2\eta r}\frac{dp}{d\theta}h$) also increases in magnitude due to the larger film thickness ($h$) within the groove region. This pressure term opposes the Couette flow term at $z$=0. Consequently, the increase in the opposing Poiseuille flow term effectively counteracts the reduction in the Couette flow term. This leads to a relatively unchanged or slightly stable overall shear rate ($du_\theta/dz$) at the bearing surface, and thus, the friction remains virtually unaffected by the groove dimensions. In contrast, at the runner surface ($z$=$h$), both the Couette and Poiseuille terms are generally positive, leading to a net reduction in the overall friction due to other thermohydrodynamic effects. The shear strain rate of the viscous fluid is the primary factor influencing friction at a moving surface, and the reduction in frictional force is attributed to a decrease in the shear strain rate. Given that the oil film thickness between the runner surface and the groove surface increases, the gradient of surface velocity with respect to oil film thickness decreases, leading to a reduction in the shear strain rate. Consequently, the overall frictional torque at the runner surface diminishes with increasing groove size. However, the results presented in Figure 11 pertain to a fixed bearing clearance. A disadvantage of this bearing configuration is the potential for high-pressure buildup exceeding the external load. Employing a free bearing clearance can mitigate this limitation by allowing adjustment of the bearing gap to generate sufficient pressure for varying external loads. Therefore, investigating the performance of bearings with v-grooves under free-bearing-clearance conditions warrants further study.

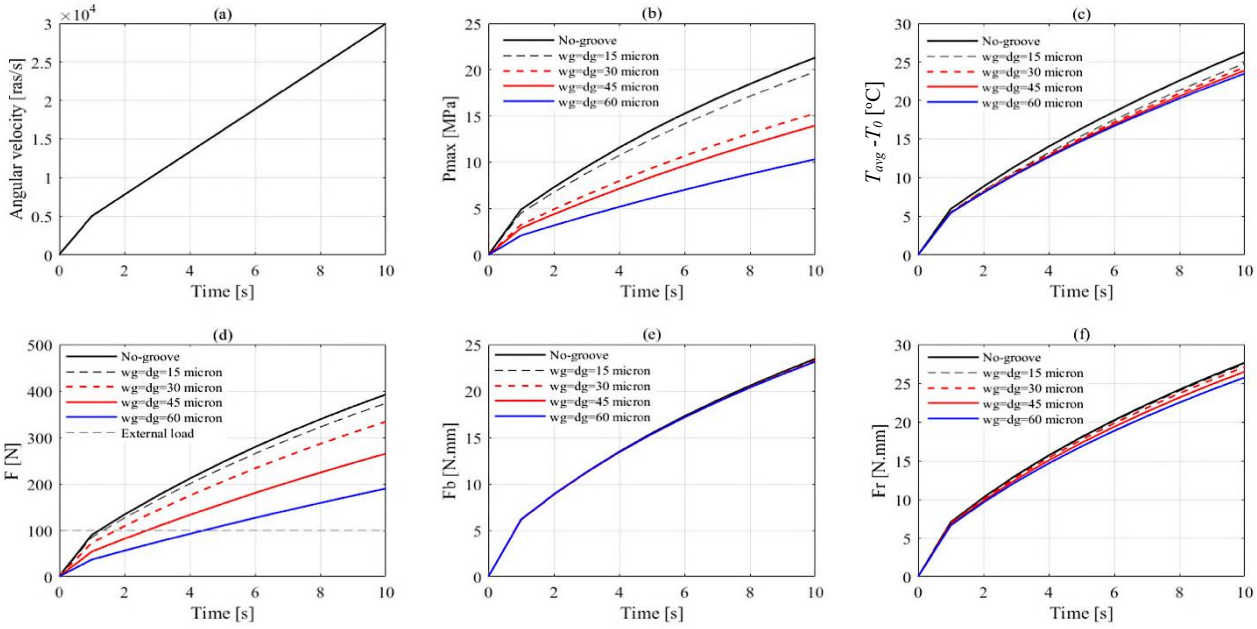


Figure 11. Characteristics of a bearing with v-grooves under fixed bearing clearance ($h_0$=5 µm, $r_{g1}$=4.25 mm, $r_{g2}$=5.25 mm): (a) rotational speed, (b) maximum pressure, (c) average increased temperature, (d) load capacity, (e) frictional torque at a bearing surface, and (f) frictional torque at a runner surface

Thrust bearing designs with free bearing clearances can be addressed by either incorporating controlled axial movement (in the micron range) during assembly or by utilizing a pivoted-pad slider bearing. The free bearing clearance analysis presented in Figures 12 and 13 relies on the assumption that the assembled thrust bearing allows for slight axial movement. This axial compliance enables the bearing clearance to adjust proportionally to the external axial load. Figure 12 illustrates the bearing behavior under consideration of free clearance conditions by comparing grooveless bearings with grooved bearings of two different sizes: 30 microns (width and depth) and 60 microns (width and depth). Figure 12(a) depicts the increasing shaft speed during turbocharger operation, while Figure 12(b) shows that the bearing is subjected to a constant external axial load of 100 N (grey line). The data indicate that all tested bearings generate sufficient force to support this external axial load and maintain equilibrium under accelerating shaft speed. As shaft speed increases, the oil pressure rises, as previously discussed (see Figure 10). To balance the axial force, the bearing clearance, or minimum film thickness ($h_{min}$), adjusts to create a supporting force that counteracts the external axial load, as shown in Figure 12(c). Notably, the bearing with 60-micron grooves exhibits the lowest bearing clearance to compensate for the pressure loss within the groove area. In contrast, the bearing with 30-micron grooves maintains a clearance level similar to that of the grooveless bearing. While increased shaft speed leads to higher oil pressure, a larger bearing clearance results in lower oil pressure. This inverse relationship allows the bearing to maintain axial force balance. Consequently,

the maximum oil pressure, as presented in Figure 12(d), remains at a relatively constant level and is not excessively high, except for the bearing with 60-micron grooves. During the initial phase of turbocharger operation (0-2 seconds), the shaft speed is low. In the bearing with the larger groove (60 microns), greater oil pressure loss occurs within the groove. Consequently, the bearing clearance at the start of operation is lower than that in other studied configurations. This reduced initial clearance results in an immediate, significantly higher peak pressure than in the other cases. Owing to the smaller bearing clearance and higher peak pressure compared to the other studied configurations, the bearing with the 60 µm groove exhibits higher frictional torque at the runner surface and a greater maximum temperature rise, as illustrated in Figures 12(e-f), respectively. Conversely, the bearing with the 30 µm groove and the grooveless bearing show comparable values for frictional torque and maximum temperature rise.

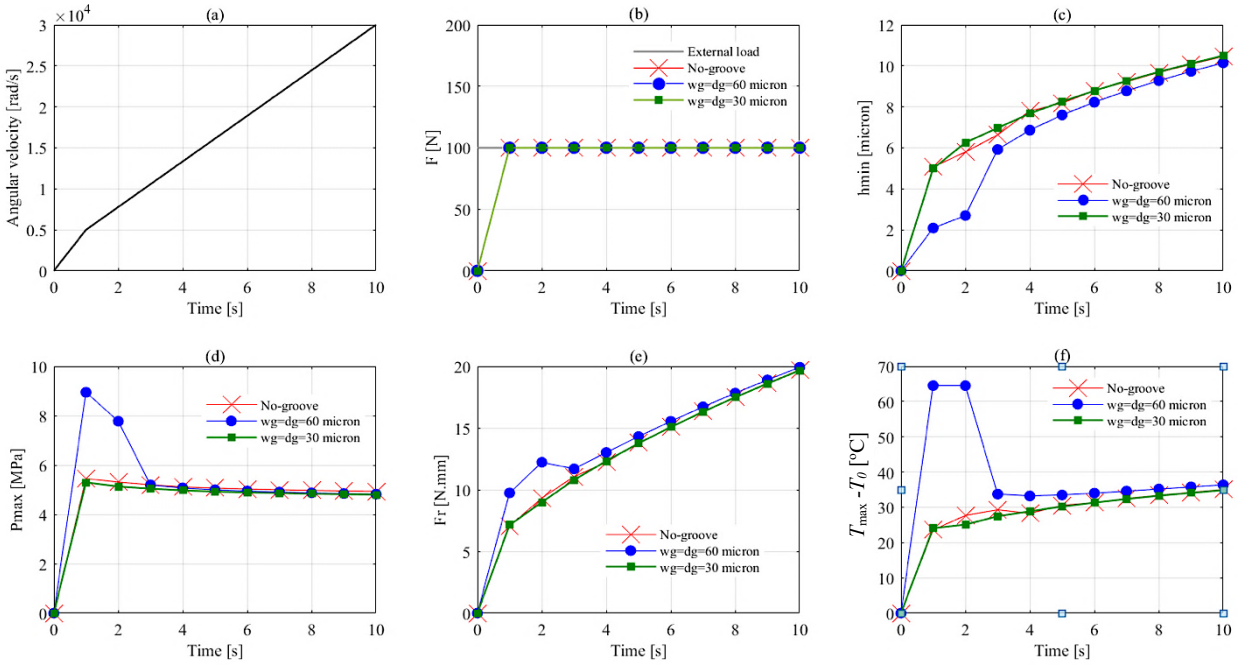


Figure 12. Characteristics of a bearing with v-grooves under free bearing clearance ($r_{g1}$=4.25 mm, $r_{g2}$=5.25 mm): (a) rotational speed, (b) axial load, (c) minimum film thickness, (d) maximum pressure, (e) frictional torque at a runner surface, and (f) maximum increased temperature

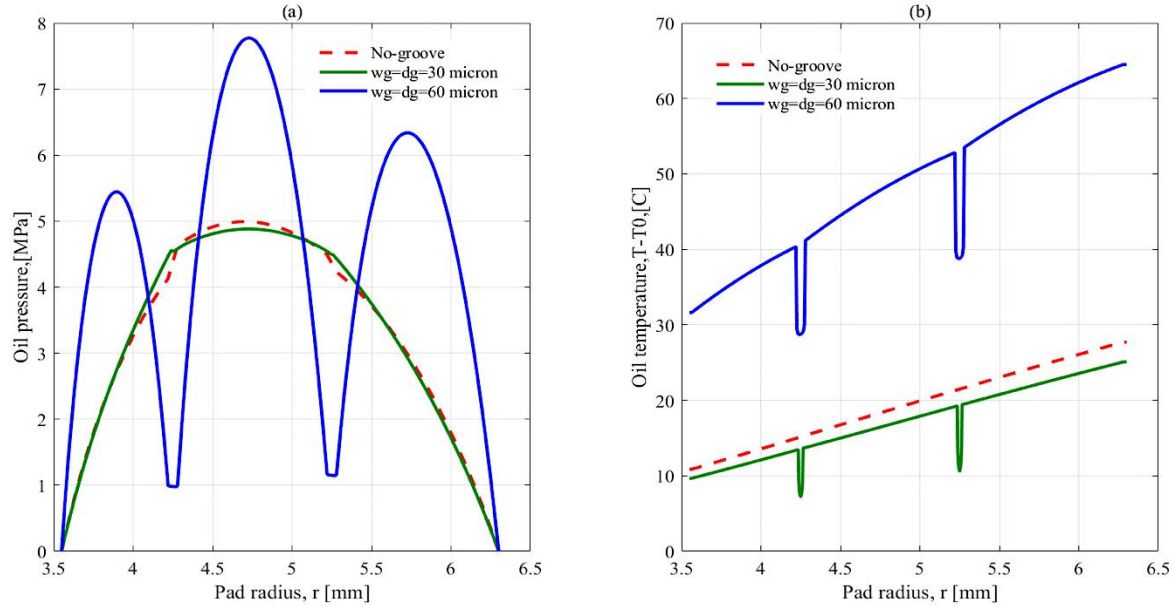


Figure 13. Comparison of thrust bearing behaviour under free bearing clearance ($t$ = 2s, external axial load = 100 N): (a) oil pressure at $\theta$= π/6 rad, (b) oil temperature at $\theta$=π/4 rad

Supporting the above explanation, Figure 13(a) presents the oil pressure distribution, and Figure 13(b) shows the temperature distribution within the transverse bearing (section B-B). Analysis of the oil pressure distribution (Figure 13(a)), captured at a pad angle of π/6 rad and a time of 2 s, indicates a substantial pressure reduction within the groove area for the 60 µm groove bearing. Higher pressures in the remaining bearing regions accompany this pressure drop. Furthermore, the 30 µm groove bearing shows a slightly reduced pressure at the plate center when compared to the

bearing without a groove. The higher pressure and thinner oil film thickness in the 60 μm groove bearing case (relative to Figure 12(c)) directly contribute to the substantially elevated temperature distribution illustrated in Figure 13(b) when compared to the other cases. Regarding oil temperature distribution, 30 μm groove bearings offer an advantage over their 60 μm counterparts and closely approximate the performance of non-groove bearings. Notably, they exhibit the lowest temperatures, with sharp drops specifically within the groove region.

The analysis of groove dimensions for both fixed and free bearing clearances under the specified turbocharger operating conditions reveals that the optimum groove width and depth should not exceed 30 μm. Exceeding this optimal dimension leads to a significant reduction in the bearing's load-carrying capacity. In practical applications where external axial forces may exceed expected limits, this reduced load capacity could lead to premature wear of the bearing or adjacent components (e.g., mounting points). Therefore, designers must predict or specify the appropriate external axial force corresponding to the selected groove dimensions. Based on the results presented herein, the recommended maximum axial force for a groove with 30 μm width and depth should not exceed 100 N. It is important to acknowledge the limitations of the current model, particularly the two-dimensional hydrodynamic assumption. This simplification excludes complex three-dimensional effects, such as cavitation and heat conduction across the film thickness. Although the thermal characteristics were captured in 3D through the energy equation, the hydrodynamic analysis remains restricted by the two-dimensional Generalized Reynolds Equation, which relies on the thin-film assumption. Future work should therefore focus on implementing a Full 3D computational fluid dynamics model based on the Navier-Stokes equations to fully account for inertial effects and complex flow structures within the film.

## 4. Conclusions

This research successfully achieved its primary objective by investigating the thermohydrodynamic characteristics of the circumferential V-groove under transient operating conditions, thereby filling a critical gap in the existing literature, which predominantly focused on steady-state analysis and did not address this specific V-groove design. The analytical results can be summarized as follows:

i) Under fixed bearing clearance conditions, the V-groove bearing demonstrated a significant reduction in oil pressure, friction, and groove surface temperature. This resulted in a lower overall average oil temperature compared to the grooveless bearing configuration.
ii) With variable bearing clearance, bearings with excessively large groove dimensions (60 μm) resulted in a diminished axial load-carrying capacity. This, in turn, caused an excessive reduction in bearing clearance, resulting in elevated operating temperatures compared to other tested configurations.
iii) The application of thrust bearings with V-groove dimensions optimized (30 μm) for the operational parameters of turbochargers presents potential for reducing oil temperature. Crucially, for this optimal configuration, the external axial force should not exceed 100 N to prevent excessive loss of load-carrying capacity and maintain safe operating clearance.

**Acknowledgements**

The author gratefully acknowledges the Department of Mechanical Engineering, Faculty of Engineering, Burapha University, for providing the research facilities that supported this work.

**Funding**

This study was not supported by any grants from funding bodies in the public, private, or not-for-profit sectors.

**Declaration of Competing Interest**

The author declares no conflicts of interest.

**CRediT Authorship Contribution Statement**

Puttha Jeenkour: Methodology, Numerical Investigation, Draft Preparation, Reviewing, and Editing

**Availability of Data and Materials**

The data supporting this study's findings are available on request from the corresponding author.

**Ethics Declarations**

This study did not involve human participants or animals. Ethical approval was therefore not required.

**Generative Artificial Intelligence Declarations**

The authors claim that artificially intelligent-assisted technologies, such as generative AI, were not used to generate content, ideas, or theories. We have just utilized AI to enhance readability and refine the language. This was used with extreme human control and oversight. The authors take full responsibility for reviewing and approving the content.

**References**

[1] B. J. Hamrock, S. R. Schmid, and B. O. Jacobson. Fundamentals of Fluid Film Lubrication, 2nd ed. CRC Press, 2004.

[2] A. Boretti, "Super turbocharging the direct injection diesel engine," *Nonlinear Engineering*, vol. 7, no. 1, pp. 17-27, 2018.
[3] F.A. Najar, G.A. Harmain, "Numerical investigation of pressure profile in hydrodynamic lubrication thrust bearing," *International Scholarly Research Notices*, vol. 2014, p. 157615, 2014
[4] A.N. Farooq, G.A. Harmain, "Performance characteristic in hydrodynamic water cooled thrust bearings," *Jurnal Tribologi*, vol. 10, pp. 28-47, 2016.
[5] K. Katsaros P. Nikolakopoulos, "On the tilting-pad thrust bearings hydrodynamic lubrication under combined numerical and machine learning techniques," *Lubrication Science*, vol. 33, no. 3, pp. 153-170, 2021.
[6] E. K. Elsayed, H. Sayed, T. A. El-Sayed, "Analysis of second-order thrust bearing coefficients considering misalignment effect," *Journal of Vibration Engineering & Technologies*, vol. 12, pp. 1957–1977, 2024.
[7] S. Gao, Y. Shang, Q. Gao, L. Lu, M. Zhu, Y. Sun, et al., "CFD-based investigation on effects of orifice length–diameter ratio for the design of hydrostatic thrust bearings," *Applied Sciences*, vol.11, p. 959, 2021.
[8] K. Pu, F. Yuan, P. Du, B. Huang, D. Fei, "Study on influence of pad surface defects on lubrication characteristics of thrust bearing," *Annals of Nuclear Energy*, vol. 203, p. 110492, 2024.
[9] J.P. Shao, G.D. Liu, X. Yu, "Simulation and experiment on pressure field characteristics of hydrostatic hydrodynamic hybrid thrust bearings," *Industrial Lubrication and Tribology*, vol. 71, No. 1, pp. 102-108, 2019.
[10] I. Syafaat, A. Nugroho, M. Sodikin, A. A. Hida, R.D. Ratnani, B. Setiyana, et al., "A 3D design of the hydrodynamic pocketed thrust bearing with slip engineered for eliminating cavitation," *Results in Engineering*, vol. 24, p. 24, 2024.
[11] I. Syafaat, R.A. Ababil, R.C. Gunawan, M. Tauviqirrahman, M. Muchammad, E. Yohana, et al., "Study of slip and cavitation condition in the open pocket hydrodynamic thrust bearing," *Jurnal Tribologi*, vol. 37, pp. 58-75, 2023.
[12] U.P. Singh, P. Sinha, M. Kumar, "Analysis of hydrostatic rough thrust bearing lubricated with Rabinowitsch fluid considering fluid inertia in supply region," *Proceedings of the Institution of Mechanical Engineers*, *Part J*, vol. 235, no. 2, pp. 386-395, 2020.
[13] W. Ouyang, Z. Yan, X. Zhou, B. Luo, B. Wang, and J. Huang, "A thermal hydrodynamic model for emulsified oil-lubricated tilting-pad thrust bearings," *Lubricants*, vol. 11, no. 12, pp. 529, 2023.
[14] H. Feng, S. Jiang, A. Ji, "Investigations of the static and dynamic characteristics of water-lubricated hydrodynamic journal bearing considering turbulent, thermohydrodynamic and misaligned effects," *Tribology International*, vol. 130, pp. 245-260, 2019.
[15] I. Chatzisavvas, A. Boyaci, A. Lehn, M. Mahner, B. Schweizer, P. Koutsovasilis, "On the influence of thrust bearings on the nonlinear rotor vibrations of turbochargers," *ASME Turbo Expo 2016: Turbomachinery Technical Conference and Exposition*, *Seoul, South Korea*, pp. 1-10, 2016.
[16] I. Chatzisavvas, A. Boyaci, P. Koutsovasilis, B. Schweizer, "Influence of hydrodynamic thrust bearings on the nonlinear oscillations of high-speed rotors," *Journal of Sound and Vibration*, vol. 380, pp. 224-241, 2016.
[17] R. Wu, B. Duan, F. Liu, H. Wu, Y. Cheng, X. Luo, "Design of a hydro-dynamically levitated centrifugal micro-pump for the active liquid cooling system," *2017 18th International Conference on Electronic Packaging Technology, Harbin, China*, pp. 402-406, 2017.
[18] B. Yang, S. Feng, J. Tian, L. Yu, "Theoretical and numerical analysis on the load capacity of hydrodynamic thrust bearings with fourier series decomposition," *2019 IEEE International Conference on Mechatronics and Automation, Tianjin, China*, pp. 2363-2368, 2019.
[19] B. Hoepke, T. Uhlmann, S. Pischinger, B. Lüddecke, D. Filsinger, "Analysis of thrust bearing impact on friction losses in automotive turbochargers," *Journal of Engineering for Gas Turbines and Power*, vol. 137, no. 8, p. 8, 2015.
[20] L. Wang, R. Zou, J. Duan, M. Chen, "Performance analysis of tilting pad thrust bearing incorporating the surface roughness, texture, and turbulence effect," *Proceedings of the Institution of Mechanical Engineers, Part J*, vol.238, no. 4, pp.390-398, 2023.
[21] X. H. Zhang, K.R. Li, H. Yan, L.W. Zheng, C.L. Ke, B. Dong, et al., "Experimental study of different structural parameters on gas lubricated spiral groove thrust bearing for cryogenic turbo expander," *IOP Conference Series: Materials Science and Engineering*, vol. 1240, p. 8, 2022.
[22] X. Lin, R. Wang, S. Zhang, S. Jiang, "Study on dynamic characteristics for high-speed water-lubricated spiral groove thrust bearing considering cavitating effect," *Tribology International*, vol. 143, p. 106022, 2020.
[23] X. Lin, S. Wang, S. Jiang, S. Zhang, "Dynamic characteristics of high-speed water-lubricated spiral groove thrust bearing based on turbulent cavitating flow lubrication model," *Chinese Journal of Mechanical Engineering*, vol. 35, no. 13, p. 21, 2022.
[24] C. Xiong, B. Xu, H. Yu, Z. Huang, Z. Chen, "A thermo-elastic-hydrodynamic model for air foil thrust bearings considering thermal seizure and failure analyses," *Tribology International*, vol. 183, p. 108373,2023.
[25] Q. Gao, W. Sun, J. Zhang, "Thermo-elasto-hydrodynamic analysis of a specific multi-layer gas foil thrust bearing under thermal-fluid–solid coupling," *Chinese Journal of Aeronautics*, vol. 36, no. 12, pp. 231-246, 2023.
[26] B. Hu, A. Hou, R. Deng, R. Wang, Z. Wu, Q. Ni, et al., "Numerical investigation of bump foil configurations effect on gas foil thrust bearing performance based on a thermos-elastic-hydrodynamic model," *Lubricants*, vol. 11, no. 10,p. 417, 2023.

[27] W.F. Chong, C.T. Lee, M.B. Lee, "Simulating thermos-hydrodynamic lubrication of turbocharger journal bearing," *Jurnal Tribologi*, vol. 30, pp. 13-23, 2021.
[28] J. Dong, H. Wen, J. Zhu, J. Guo, C. Zong, "Analysis of thermo-hydrodynamic lubrication of three-lobe semi-floating ring bearing considering temperature–Viscosity effect and static pressure flow," *Lubricants*, vol. 12, no. 4, p. 140, 2024.
[29] J.A. Bhat, G.A. Harmain, M.F. Wani, R. Sehgal, F.A. Najar, "Performance enhancement of hydrodynamic thrust bearings: Investigating cooling strategies, deep recesses, and textured surfaces," *Tribology International*, vol. 211, p. 110877, 2025.
[30] K. Boonlong, P.Jeenkour, "Experimental Study on Oil Pressures of Hydrodynamic Lubrication in Thrust Bearing Considering Circumferential V-Grooved Pad," *International Journal of Mechanical Engineering and Robotics Research*, vol. 9, no. 3, pp. 453-458, 2020.
[31] I. Chatzisavvas, "*Efficient thermohydrodynamic radial and thrust bearing modeling for transient rotor dimulations*," Ph.D. dissertation, Technische Universität Darmstadt, Darmstadt, Germany, 2018.